Available online at www.sciencedirect.com
ScienceDirect
International Journal of Thermal Sciences 48 (2009) 554–572
International Journal of Thermal Sciences
www.elsevier.com/locate/ijts

The role of droplet fragmentation in high-pressure evaporating diesel sprays

S. Tonini [a,c], M. Gavaises [a,*], A. Theodorakakos [b]

[a] *School of Engineering and Mathematical Sciences, City University London, UK*
[b] *Fluid Research Co., Athens, Greece*
[c] *Presently at Industrial Engineering Department, Università di Bergamo, Italy*

Received 29 November 2007; received in revised form 28 February 2008; accepted 25 March 2008

Available online 25 April 2008

Abstract

The relative importance of the physical processes taking place during the development of Diesel sprays is evaluated through use of a dense-particle Eulerian–Lagrangian model. The physical processes considered include the influence of the injection conditions, as determined by a nozzle cavitating flow model, liquid-core atomisation, droplet break-up, turbulent dispersion, droplet-to-droplet interactions and vaporisation. For the latter, different physical mechanisms are included, considering high pressure and temperature as well as multi-component effects. Droplet aerodynamically-induced break-up is the dominant mechanism determining the contact area between the droplets and the surrounding air during their fragmentation period. Furthermore, a new model is considered for the droplet deformation induced during the fragmentation processes of the moving droplets. That is found to increase substantially the interface area available for heat transfer and vaporisation and to reproduce the observed trend of liquid penetration being independent of injection pressure. Model predictions are successfully compared against a wide range of experimental data for the liquid and vapour penetration, spray CCD (Charge Coupled Device) images and PDA (Phase Doppler Anemometry) measurements for various injector nozzle geometries. The results are found to predict trends as well as actual values of the penetrating fuel plumes, as function of nozzle geometry, injection pressure and air thermodynamic conditions covering the range of conditions of modern supercharged DI Diesel engines.

Keywords: Diesel sprays; Dense spray modelling; Nozzle cavitation; PDA measurements; Droplet break-up; Fuel vaporisation

1. Introduction

Over the last few years the high-speed direct injection (DI) Diesel engine has become an alternative to the gasoline engine for modern passenger car applications. Good drivability and durability together with unrivalled fuel economy has led to its increasing popularity in the European market where cars powered by DI Diesel engines now enjoy 40% of the total market share. The high speed direct-injection (HSDI) Diesel engine has been shown to give 15% lower fuel consumption than indirect injection Diesels and ∼ 20% savings when compared to gasoline direct injection (GDI) engines. In the commercial sector, the heavy-duty DI Diesel engine is the power plant of choice. It is well known that the performance and exhaust emissions of DI Diesel engines are strongly affected by the nozzle flow exit characteristics, which control the atomisation process of the injected fuel and the subsequent spray development [1]. Under most operating conditions cavitation occurs inside the injector nozzle [2]; this is generally accepted as one of the most important parameters affecting fuel spray atomisation [3, 4]. Laser-based experimental techniques, for example [5], have been extensively applied as diagnostic tools in characterising the transient development of high-speed sprays. However, due to the very short time scales of the underlying processes and the very large number of droplets present, the link with the internal nozzle flow during the injection period remains still a grey area. Moreover, simultaneous imaging of the internal nozzle flow and the spray is very difficult; thus, up to now relevant information is mainly based on computational models.

An increasing number of numerical models have appeared in the literature, which allow the effect of nozzle cavitation to be simulated, representative studies are those reported by [6–

* Corresponding author.
E-mail address: m.gavaises@city.ac.uk (M. Gavaises).

1290-0729/$ – see front matter
doi:10.1016/j.ijthermalsci.2008.03.020

Nomenclature

Greek symbols

α	volume fraction
β	non-dimensional parameter
ΔH	latent heat
Δt	time step
ϕ	fugacity coefficients
Λ_K	Knudsen layer thickness
μ	dynamic viscosity
π	Pi-Greek
ρ	density
σ	surface tension
$\sigma\delta$	standard deviation
τ	non-dimensional time

Roman symbols

A	area
a, b	equation of state coefficients
B_M	Spalding mass transfer number
C	model constant
C_D	drag coefficient
Cp	heat capacity at constant pressure
D	diameter
$diff$	diffusion coefficient
$\mathbf{F}$	force vector
h	convective heat transfer coefficient
m	mass
$\dot{m}$	vaporisation rate
mw	molecular weight
N	number
Oh	Ohnesorge number
P	pressure
$\dot{Q}$	instantaneous volume flow rate
R^*	universal gas constant
R	radius
Re	Reynolds number
Sh	Sherwood number
sp	spray penetration
t	time
T	temperature
u	velocity vector module
$\mathbf{u}$	velocity vector
V	volume
We	Weber number
y	mass fraction
Y	molar fraction
Z	compressibility factor

Subscript

aerod	aerodynamic
atm	atmospheric
b	boiling
back	chamber condition
break	break-up
crit	critical
def	deformation
eff	effective
evap	evaporative
fc	fragment cloud
g	gas
inj	injection
jet	liquid ligament exiting the nozzle
l	liquid
max	maximum
non-eq	non equilibrium
p	particle
P	parcel
ref	reference
rel	relative
sph	spherical
st	stable
strip	stripping
surf	surface
tot	total
v	vapour
∞	surrounding conditions

Superscript

$'$	fluctuating component

9], while at the same time simultaneous solution of the internal nozzle flow with the injected spray can be achieved. Computational fluid dynamics (CFD) has become an integral part of the analysis and design of automotive products. Recent advances in the relevant software together with computer hardware enable time-dependent flows within complex geometries to be calculated in a cost efficient way [10–12]. It is generally accepted that accurate modelling of the interaction of flows with sprays is a key factor in simulating the whole engine flow and combustion processes. The well-known Eulerian–Lagrangian numerical approximation frequently adopted for prediction of the multi-phase flow processes in internal combustion engines has been extensively discussed in the past, for example by [13–17]. It is based on the assumption that the injected liquid can be simulated as a dispersed phase through tracking of the trajectories of a sufficient number of representative parcels moving in the carrier gas. The later is modelled as a continuous phase using an Eulerian approach. The stochastic particle method proposed in [18] is usually implemented to account for the dispersed phase development on a Lagrangian frame of reference, where the properties of the representative droplets are randomly chosen from empirical/calculated distribution functions. With this methodology, phenomenological sub-models are required to account the various physical processes taking place in the sub-grid time and length scales. Recently, a hybrid-approach has been developed in [19]. This method combines a Large Eddy Sim-

ulation (LES) model for the prediction of turbulent transport properties, also used for estimating the maximum stable diameter of droplets before break-up, with the standard Lagrangian model for predicting atomisation and spray evolution; the authors demonstrated that satisfactory predictions for the spray development can be obtained particularly in complex configurations with the presence of large number of droplets close to the injector. The work presented in [20] has concluded that the physical sub-models related to spray processes employed for in-cylinder CFD calculations are still inadequate from being fully predictive and require tuning. These processes are influenced by a variety of parameters like the nozzle geometry, the characteristics of the fuel supply system and the liquid–gas aerodynamic interaction.

Recent modelling efforts have lead to successful coupling of the local flow conditions at the injector exit with advanced primary break-up models that include injector flow induced turbulence as well as cavitation effects on the liquid fragmentation processes. Liquid primary and secondary break-up models, which account for the competing effect of turbulence, cavitation and aerodynamic induced fragmentation processes, are based upon the spatially and temporally resolved injector flow data at the nozzle exit. Initial turbulence length scales have been found to have a strong influence also on the prediction of gas phase penetration under evaporating conditions, according to [21]. In order to provide CFD users with accurate droplet size spectra for secondary break-up sub-models, as function of the injection velocity, mean turbulence levels, liquid–gas density ratio and injector diameter, a two-dimensional (2D) Volume of Fluid (VOF)—LES model has been proposed in [22], which was then extended to a more realistic three-dimensional (3D) one [23, 24]; this methodology simulates the liquid jet atomisation from first principles. However, the enormous calculation time, of the order of few weeks even with parallel computations, limits such models to cell sizes grater than 4 μm (i.e. droplets greater than 15 μm), which is not enough to resolve the full droplet size distribution of Diesel sprays. In addition, these models, although they use the information of the internal nozzle flow, have not been applied yet to realistic 3D nozzle designs where cavitation dominates the flow distribution. Furthermore, [25] and [26] provided noticeable information on the liquid core structure and spray morphology at the nozzle exit. It is thus not surprising why most of the commercial CFD codes for spray simulations employ phenomenological atomisation models, irrespectively if an Eulerian–Eulerian or Eulerian–Lagrangian method is used, for example see [27]. Still, the favourable approach is the Lagrangian one since it can be easily coupled with vaporisation and eventually combustion models [28]. Although this method has been introduced to specifically characterise dilute sprays, numerical shortcomings have been overcome in recently published studies, for example [29] and [30], where multi-phase Eulerian–Eulerian are combined with Lagrangian models after fuel atomisation (referred to hybrid models). An alternative dense-droplet Lagrangian model described by [31] has been also proved to result in grid independent solutions for grids refined down to sizes equivalent to those of the droplet parcels. Thus, this numerical methodology can be used to assess the effect of the physical sub-models resolving the sub-grid scale processes.

The present paper is a continuation of the recent work of the authors reported in [31] and [32]. In this work, aspects of the numerical implementation of the method have been presented, demonstrating its minimum dependency on the numerical grid and the temporal and spatial discretisation schemes. The present paper validates the relevant sub-grid length and time scale physical sub-models being an integral part of the whole spray model and accounting for fuel injection, droplet primary and secondary break-up, vaporisation, droplet turbulent dispersion and droplet-to-droplet interactions; in addition, their relative influence on the overall spray characteristics is investigated and quantified for a number of injection and surrounding air thermodynamic conditions of practical importance. Special emphasis is given here to the influence of droplet aerodynamic deformation, which eventually leads to droplet break-up, on the vaporisation processes. The latter has been modelled following different assumptions, including high pressure, temperature and non equilibrium effects [33,34], in addition to a model accounting for multi-component liquids [35]; however, the findings from the present investigation suggest that the most influential factor for predicting the correct trend of evaporating Diesel sprays is the increased surface area between the liquid droplets and the surrounding air formed during their fragmentation processes. This has allowed calculation of liquid penetration length independent of the injection pressure, which is one of the well-known characteristics of such sprays. Model predictions are extensively validated against experimental data and presented consistently for the first time here. These have included liquid and vapour spray tip penetration, spray CCD images and PDA measurements obtained for cavitating and non-cavitating single- and multi-hole nozzle designs for a wide range of operating conditions. Limited droplet size and velocity measurements reported by [36], [37] and [38] for two types of multi-hole nozzles under non-evaporating and moderately evaporating conditions have been used for validation of the droplet size and velocity. Successively, the experimental data reported by [39] for the liquid and vapour penetration of evaporating Diesel sprays are used to assess the physical effect of the various spray sub-models both for cavitating and non-cavitating nozzles; predictions for sprays injected from the same injector nozzle and identical operating conditions in a non-evaporating quiescent environment are also used to guarantee the validity of the model under room temperature conditions. Finally, the model is validated against the experimental data base of [40] for single-hole injectors under a variety of injection pressures, back pressures and temperatures, injection hole diameters and fuel initial temperature and composition.

2. Test cases

In this section the test cases performed for the purposes of the present investigation are described. Although emphasis is placed on the role of droplet fragmentation under evaporating conditions, it has been considered essential to validate the model under non-evaporating conditions. Thus, the

Table 1
Operating conditions for the PLN (Pump Line Nozzle) injection system connected to inclined sac-type nozzle and CR (Common-Rail) system connected to vertical VCO nozzle; the schematic shows the PDA measurement points where droplet velocity and size measurements have been obtained at 10, 20, 30 and 40 mm from the nozzle hole exit on the centreline

Case	1	2
Fuel Injection Equipment	PLN–Sac	CR–VCO
Orifice diameter (mm)	5 × 0.22	5 × 0.172
Peak injection pressure (bar)	800	1200
Fuel delivery (mm^3/stroke/hole)	4	4
P_{back} (bar)	1	17.2
T_{back} (K)	300	500

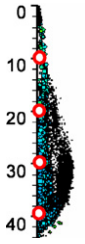

test cases used are divided into three groups. For the first one limited measurements for the droplet size and velocity under non-evaporating and moderate evaporating air conditions are used; the corresponding predictions are presented in this section of the paper. Then the 2nd group of test cases is described; this assesses the model against evaporating as well as non-evaporating conditions, giving emphasis on the relative influence of droplet fragmentation on the vaporisation process both for non-cavitating and cavitation nozzle designs. Finally, the 3rd group of test cases validates the model under a wide range of air thermodynamic conditions, fuel composition and nozzle design.

2.1. Droplet velocity and size validation test cases

At first, results used for model validation are those reported by [36] and [37]. These refer to sprays injected with relatively low injection pressure under atmospheric air conditions. They have been selected for model validation since there is detailed information available regarding the whole fuel injection system and the internal nozzle geometry, line pressure, needle lift and fuel injection rate. Details for the injection conditions required as input to the spray can be found in [14]. Case 1 of Table 1 presents the operating conditions investigated and a schematic of the PDA measurement points where droplet velocity and size have been obtained at 10, 20, 30 and 40 mm from the nozzle hole exit on the spray centreline. The Diesel fuel is modelled using the physical properties of *n*-dodecane. The experimental data provide information for the temporal and spatial droplet velocity and size distributions. The fuelling was approximately 4 mm^3 per hole and per stroke, while the injection duration was around 0.8 ms. Two peak injection pressures of 800 and 1200 bar have been selected, while more detailed about the nominal rail pressures can been found in [36] and [37]. Simulations have been performed using the standard model settings which will be described in detail in the following section of the paper and are also listed in Table 5. Comparison between computational and experimental results is presented in Fig. 1 for the 800 bar peak injection pressures case. Satisfactory agreement between measurements and computations can be appreciated. The model is able to predict the velocity increase during the initial stage of injection, which lasts up to 0.4 ms and which coincides with the corresponding increase of the injection pressure and flow rate traces within the fuel injection system. The

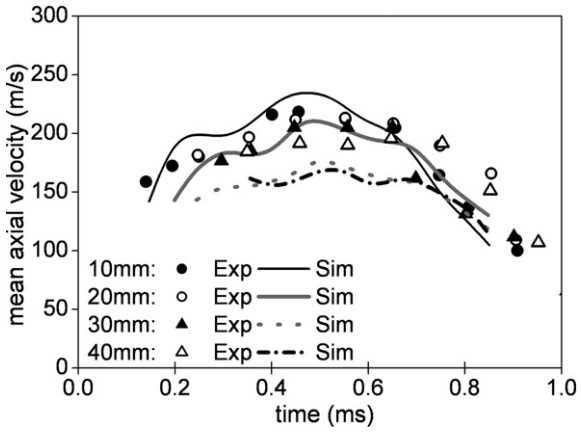

Fig. 1. Comparison between PDA measurements [36,37] and model predictions for the droplet mean axial velocity component at 10, 20, 30 and 40 mm from the nozzle exit under quiescent atmospheric conditions; case 1 of Table 1, standard model settings.

peak droplet velocity decreases from 250 m/s down to 200 m/s as the spray penetrates downstream of the hole exit due to droplet aerodynamic drag. Although not presented in this graph, it has to be noted that predictions obtained by neglecting the velocity increase caused by nozzle cavitation have resulted up to 30% underestimation of the droplet velocity [41]. Thus, nozzle hole cavitation plays an important role for injection under atmospheric conditions.

Additional droplet size and velocity measurements have been reported by [38] for injection into a high pressure/temperature chamber, which represents an extension of the above described test case; the conditions tested are summarised as case 2 in Table1. The total fuelling was again approximately 4 mm^3 per injection stroke per hole, with peak rail pressure of 1200 bar. Injection was taking place against compressed nitrogen at 17.2 bar and 500 K back temperature in order to reproduce moderate evaporating environments. It has to be noted that for the data reported for multi-hole nozzles, the needle valve opening and closing has been considered while formation of cavitation inside the nozzle was also simulated in a transient mode. Fig. 2 presents a comparison between model predictions and experimental data for the temporal variation of the spray SMD at two points across the spray, located 2 and 3 mm from the centreline and at 12.5 mm downstream from the nozzle hole exit; this was the nearest distance from the hole location

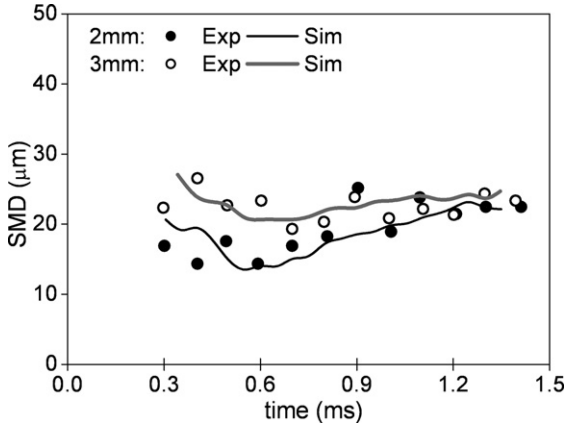

Fig. 2. Comparison between PDA measurements [38] and model predictions for the droplet SMD at two points across the spray, located 2 and 3 mm from the centreline and 12.5 mm from the nozzle hole exit for evaporating spray conditions; case 2 of Table 1, standard model settings.

where measurements were available. The graphs show reasonable agreement between PDA measurements and calculations. It has to be noted that up to this distance, which is almost 70 nozzle diameters downstream of the nozzle exit, the liquid core atomisation has been already completed and the secondary droplet break-up is the most important spray processes taking place. Droplet size SMD values are in the range of 20 μm, as both measurements and model predictions indicate. Predictions show an initial decrease of the droplet size during the early stages of injection, which is attributed to the increase of the injection velocity during the early stages of injection. Further on, once quasi-steady-state conditions have been reached near the nozzle exit, an increase in the droplet size is observed both in measurements and model predictions. This is due to the aforementioned decrease of the relative velocity between the two phases, which leads to the formation of relatively larger droplets during droplet break-up events. This variation seems to be more evident for the location closer to the nozzle exit while at the 3 mm point, located on the periphery of the spray, a more uniform droplet size is measured and predicted during the injection period.

Having validated the spray model for injection into non-evaporating and moderate evaporating environments, we proceed to the description of the test cases forming the core of the present investigation.

2.2. Test cases against the experimental data of [39]

Use of single-hole nozzles simplifies significantly the internal nozzle flow structures and thus the associated effects on spray can be isolated. In particular, formation of transient vortices and string cavitation [2] is eliminated while different levels of hydrogrinding can even eliminate formation of geometrically-induced hole cavitation. As part of experimental results reported by [39], different axis-symmetric single-hole test nozzles have been manufactured and used for the spray characterisation. The first one has a sharp inlet, which enhances formation of fully developed cavitating conditions while the second has a rounded-inlet with 18% hydro-grinding. This nozzle was cavitation-free for all operating conditions investigated. Comparison of model predictions for these nozzle designs can isolate the effect of cavitation on the spray atomisation and thus allow validation of the corresponding atomisation models. For the case of the cavitating nozzle, two-phase internal nozzle flow calculations performed using rail pressure measurements and reported by [6] have provided the injection conditions used as inputs to the Eulerian–Lagrangian spray model. Injection was taking place against pressurised N_2 at 20 bar and 54 bar while the nominal rail pressure values used were 500, 800 and 1200 bar. In order to match the flow rate between the two nozzle designs, the cavitating nozzle, which has a reduced discharge coefficient around 0.7, had a hole diameter $D_{0\%\mathrm{HE}} = 209$ μm while the non-cavitating nozzle had a smaller hole diameter of $D_{18\%\mathrm{HE}} = 184$ μm and discharge coefficient equal to 0.9. More details about the fuel injection condition can be found in [32, 42]. Spray simulations have been performed under both non-evaporating (20 bar–273 K) and evaporating (54 bar–900 K) conditions. Those operating points have been selected to have the same back density, which is the main parameter controlling fuel penetration, of about 20 $\mathrm{kg/m^3}$. The cases investigated here are summarised in Table 2. These operating points have been selected to have the same air density, which is one of the main parameter controlling droplet drag coefficient and droplet aerodynamic break-up. Experimental data used for model validation include spray CCD images and the temporal variation of liquid and vapour penetration. For the particular cases investigated here, the predicted temporal variation of the SMD of the formed droplets as function of the nominal rail pressure values considered can be seen in Fig. 3. The expected size range of the formed droplets is around 15 to 20 μm at the end of injection, with smaller droplets formed with increasing injection pressure; this difference becomes smaller between the 800 and the 1200 bar cases, leading to the conclusion that the mean size of the droplets comprising the spray plume is not significantly affected when the injection pressure is sufficiently high.

Table 2
Nominal rail pressure and air thermodynamic conditions investigated for the 2D axisymmetric single-hole nozzles connected to CR system, under non-evaporating and evaporating conditions; experimental data from [39]

Case	4a, b	5a, b	6a, b	7a, b	8a, b	9a, b
Nominal rail pressure (bar)	500	800	1200	500	800	1200
Fuel delivery ($\mathrm{mm^3}$/stroke)	20	26	34	20	26	34
P_{back} (bar)	20	20	20	54	54	54
T_{back} (K)	273	273	273	900	900	900

Cases (a) refer to a 0.209 mm sharp-inlet hole and cases (b) refer to a 0.184 mm rounded-inlet hole.

2.3. Test cases against the experimental data of [40]

The last set of experimental data used for model validation has been reported by [40]. The range of conditions investigated are summarised in Table 3; as it can be seen, they cover a wide range of air density up to 60 $\mathrm{kg/m^3}$, and temperature up to 1300 K, injection pressure up to 1400 bar and nozzle hole diameter from 0.1 to 0.5 mm. Similarly to the previous experimental data base, single-hole nozzles have been utilised while

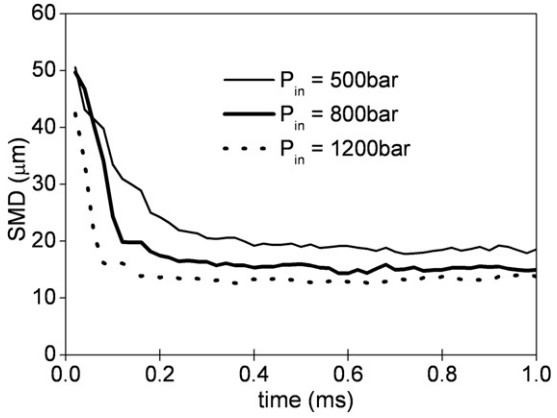

Fig. 3. Effect of injection pressure on the predicted spray SMD for the three nominal rail pressures investigated for the cavitating nozzle under non-evaporating conditions; cases 4a, 5a and 6a of Table 2.

Table 3
Summary of variation of the various parameters investigated [40]. They include a variety of nozzle hole geometric and flow characteristics, ambient pressure and temperature, fuel composition and temperature, and injection pressure

Orifice diameter (mm)	0.100, 0.246, 0.498
Area contraction coefficient	0.86, 0.81, 0.88
Discharge coefficient	0.80, 0.78, 0.84
T_a (K)	696, 700, 1000, 1007, 1295, 1300
T_{fuel} (K)	375, 410, 438
ρ_a (kg/m^3)	3.6, 14.7, 30.2, 59
ΔP (MPa)	65, 110, 135, 136, 137
Fuel	HMN, $C_{16}H_{34}$, DF2

relative long injection duration periods have been used in order to reach steady-state conditions and de-associate the spray structure from the opening and closing of the needle valve. For all cases investigated vaporisation takes place and results in a threshold level of liquid penetration for a given set of conditions. This value of liquid penetration has been referred to as 'liquid length' and has been used for model validation. The flow rate for each test case investigated has been estimated from the given pressure drop, hole orifice diameter and discharge coefficient while the injection velocity has been calculated from the reported value for the nozzle hole contraction coefficient. In the absence of a complete data base for their physical properties, the HMN fuel has been simulated with the properties of $C_{14}H_{30}$ and the cetane with those of $C_{16}H_{34}$. Finally, for the DF2 fuel the distillation curve was given in Table 4, together with the necessary fuel properties as function of temperature.

Before describing the model details, the following remarks have to be made. For most cases investigated, 2D axis-symmetric simulations have been performed since injection takes place against quiescent air. Different grids have been used to illustrate the ability of the model to resolve the spray development with almost zero dependency on important parameters of the air motion induced by the spray injections and simulated on the Eulerian grid [42]. The 2D axis-symmetric computational grid used consists of ∼50 000 cells and has a minimum cell size of 0.15 mm. As part of the parametric investigation and model validation to be presented here, a combination of

Table 4
DF2 fuel distillation curve

IBP	10%	30%	50%	70%	90%	EBP
472 K	499 K	518 K	534 K	550 K	576 K	599 K

Table 5
'Standard' settings for the spray sub-models used

Spray sub-model	Description
Atomisation	(^{1}) Cavitation-induced with radial distribution [45]
	(^{2}) Turbulence-induced without radial distribution [44]
Secondary break-up	[14]
Vaporisation	High pressure vaporisation model [33]
Drag	[66]
Turbulence dispersion	[73]
Droplet shape	Deformed

sub-models and values of empirical parameters will be referred to as 'standard' settings. These are listed in Table 5. Parametric studies for the relative influence of the different processes on the predicted results are a substantial part of the present investigation. The different models tested and compared against experimental data are shown in Table 6. Although the details will be highlighted in the following section of the paper, it can be seen that the effects tested refer to nozzle hole cavitation, evaporation, break-up, turbulent dispersion processes as well as aerodynamic drag coefficient calculation and droplet shape deviation from sphericity.

3. Model description

In the following sections the details of the CFD spray sub-models implemented in the code are presented and discussed, while the formulation of the continuous and dispersed phase governing equations can be found in [6,42]. The simulation of the continuous and disperse phases, describing the gas and liquid spray motion, is performed using the GFS (General Fluid Solver) flow code developed by the authors of the present paper, employing the RANS methodology and the standard k–ε model of turbulence. All calculations have been performed using fully unstructured numerical grids and employing local grid refinement at the area of spray development; details can be found in a recent complementary study [31].

3.1. Fuel injection

The Lagrangian methodology requires knowledge of the initial parcel velocity, size, temperature, composition and fuel injection rate transiently resolved during the injection period. In the case that the cavitation structures formed inside the nozzle reach the hole exit, the percentage hole exit cross-sectional area occupied by cavitation bubbles is also required as additional input since it determines the liquid velocity (and momentum) increase due to cavitation. In addition, the mean turbulent kinetic energy and its dissipation rate averaged over the hole cross sectional area are further integral parameters required by the atomisation models. The operation of typical Diesel fuel injection systems can be simulated with use of one-dimensional,

Table 6
Summary of the effect of spray physical sub-models on the predicted liquid and vapour penetration under non-evaporating and evaporating conditions

Spray sub-model	Description	Case	Case 6a	Case 9a	
			$\sigma\delta_{sp,l}$	$\sigma\delta_{sp,l}$	$\sigma\delta_{sp,v}$
Standard settings	Table 5	A_1	2.8	2.3	3.4
Atomisation model	No atomisation model ($SMD_{inj} = 50$ μm)	B_1	6.6	7.3	3.2
	Turbulence induced atomisation model	B_2	3.8	8.8	1.1
Break-up model	No break-up model	C_1	8.9	34.2	5.6
Drag model	Model 1 (Solid particle)	D_1	6.9	26.5	3.2
	Model 2 (Liquid spherical droplet)	D_2	6.6	26.8	3.2
	Model 3 (Void contribution)	D_3	6.8	26.7	2.9
Turbulent dispersion model	Model 1 (no turbulent dispersion)	E_1	–	2.8	3.5
	Model 3 [74]	E_2	–	5.9	3.2
	Model 4 [71]	E_3	–	1.5	3.5
Evaporation model	Ideal Equilibrium Model	F_1	–	18.7	3.1
	Non-Equilibrium Model	F_2	–	18.6	3.1
Deformation model	Spherical droplet	G_1	–	26.6	2.8

transient and compressible flow model accounting for the pressure wave dynamics in the injection system [42]. Combination of such a model with multi-dimensional and multi-phase cavitation models of Diesel nozzle flow results in prediction of the amount of cavitation vapour reaching the nozzle exit, transiently resolved during the injection period. The mass of the injected fuel is calculated from the transient fuel injection rate while the injection velocity, assumed to be uniform along the injection hole cross sectional area, is estimated from the geometric velocity and the area contraction coefficient due to the presence of cavitation bubbles, according to the following expression:

$$u_{\text{jet}} = \frac{\dot{Q}}{A_{\text{hole}} C_{\text{eff}}} \tag{1}$$

where $\dot{Q}$ is the instantaneous volume flow rate, A_{hole} the hole geometric area and C_{eff} the hole area contraction coefficient, defined as the ratio between the cross sectional area effectively occupied by the liquid and the hole geometric area; the injection direction coincides with the hole axis of symmetry. The initial parcel size is assumed to be equal to the effective hole diameter. The number of parcels injected at each computational time step is calculated from the instantaneous fuel injection rate as:

$$N_{P,\Delta t} = \frac{\dot{Q}\,\Delta t\, N_{P,\text{tot}}}{V_{P,\text{tot}}} \tag{2}$$

where $N_{P,\Delta t}$ represents the number of parcels injected during the time step Δt, and $N_{P,\text{tot}}$ and $V_{P,\text{tot}}$ stand for the total injected number of parcels and total volume of liquid injected over the whole injection duration, respectively. The injected droplets are assumed to be spherical, while their temperature is set equal to that of the fuel temperature at the exit of the nozzle; the latter may also vary during the injection period if nozzle wall heat transfer is considered in the nozzle simulation model.

3.2. Fuel atomisation

Although atomisation is the subject of numerous experimental and computational investigations, it remains a phenomenon difficult to comprehend, since it requires understanding of the link between the internal nozzle flow characteristics with the subsequent spray formation. Relevant studies have also revealed that fuel atomisation is determined by a combination of different parameters, including the liquid physical properties, the surrounding gas conditions and the type of the atomiser. A frequently adopted model for liquid jet disintegration for conditions relevant to Diesel injectors based on the linear instability analysis of aerodynamically-induced surface waves has been presented by [43]. Other models include the effect of liquid turbulence and presence of cavitation in the injector holes. In the absence of cavitation forming and reaching the nozzle hole exit, the jet turbulence-induced atomisation model, developed by [44], has been adopted here for modelling liquid atomisation. In case of cavitation forming inside the injection hole, the model proposed in [45], which considers the effect of cavitation on the disintegration of the liquid jet, is used. The model assumes that the collapsing of the cavitation bubbles emerging from the injection hole is responsible for liquid jet fragmentation. Additionally, due to turbulence dispersion of the bubbles within the liquid, vapour bursting may occur on the surface of the liquid jet before collapse.

3.3. Secondary droplet break-up

Following the disintegration of the injected liquid and the formation of droplets, aerodynamically-induced droplet break-up takes place as droplets penetrate into the surrounding air [46, 47]. Modelling of these processes is also empirical and it is based on experimental observations. The process is assumed to be controlled by the droplet Weber number expressing the ratio between inertial and surface tension forces [48] and defined as:

$$We = \frac{\rho_g \cdot D_p \cdot u_{\text{rel}}^2}{\sigma_l} \tag{3}$$

Different correlations estimating the post break-up droplet characteristics have been reported in [14], combining findings from relevant studies reported in [17] and [48–54]. The reported correlations define the mean droplet diameter and deformation process until droplet fragmentations is completed at the break-up time. Experimental findings indicate that the fragmentation

process can be classified into a number of different modes. These are usually referred to as vibrational, bag, chaotic, sheet stripping, wave crest stripping and catastrophic modes of break-up while classification is based on the droplet Weber number [53,54]:

$We < 12$	Vibrational
$12 \leqslant We < 18$	Bag
$8 < We \leqslant 45$	Bag-and-steamen
$45 < We \leqslant 100$	Chaotic
$100 < We \leqslant 350$	Sheet stripping
$350 < We \leqslant 1000$	Wave crest stripping
$1000 < We \leqslant 2670$	Catastrophic

(4)

Analysis of experimental data leads to some conclusions about the order of magnitude of break-up time, number of formed droplets, droplet sizes and deviation from sphericity. Fig. 4 shows the droplet Weber number distribution at the time of a break-up event during the whole injection period for the non-evaporating and evaporating conditions for both the low and high nominal rail pressures of Table 2. As can be seen from that plot, Weber numbers are above 100, which implies that only the stripping and the catastrophic regimes are actually taking place. The majority of the break-up events occur in the stripping mode, particularly for the lower injection pressure case where that process counts up to 90% of the recorded events. For the higher injection pressure case, about 75% of the recorded events are occurring in the range of the stripping regime and the 25% in the catastrophic mode. It has also been noticeable that break-up events do not occur only once but they dominate the droplet state within a range of distances from the nozzle exit. This can be seen in Fig. 5, which presents the probability of a break-up event as function of the distance travelled by the moving droplets. As can be seen, break-up events require some time to initiate following liquid injection, which is enough for the high velocity droplets to travel a distance up to 5 mm from the nozzle exit. Break-up events seize again at a distance between 15–20 mm from the nozzle, both for evaporating and non-evaporating conditions. This implies that below that location any recorded variation of the droplet size is mainly due to evaporation and droplet-to-droplet interactions; the latter is almost not appreciable for evaporating conditions where liquid vaporises completely at a distance of about 25 mm from the injection hole, as shown later.

During the fragmentation period, the droplet experiences deformation from its spherical shape. Since detailed simulation of the droplet shape is beyond the scope of the present investigation, its shape can be approximated by that of a spheroid having an instantaneous diameter on the elongated axis D_{def} that can take a maximum value of $D_{\text{def,max}}$ as experimental data reported by [46,48] and [50,51]. These parameters can be calculated from the following empirical correlations:

$$D_{\text{def,max}}/D_p = 1 + 0.19We^{0.5} : Oh < 0.1 \tag{5}$$

$$\frac{D_{\text{def}} - D_p}{D_{\text{def,max}} - D_p} = 0.8\frac{t}{\tau_{\text{break-end}}} \tag{6}$$

Fig. 6 shows the temporal variation of the mean droplet deformation as calculated from Eq. (6) during the development of the evaporating spray for two nominal rail pressures of 500 and 1200 bar. The curves plotted show that following liquid injection mean droplet shape deviates from the spherical one by a factor of 5, which is roughly translated to an increased contact area of approximately 7–10 times compared to that of spherical droplets. This has a profound effect on fuel vaporisation rate, which is shown in Fig. 7(a). The vaporisation rate plotted here

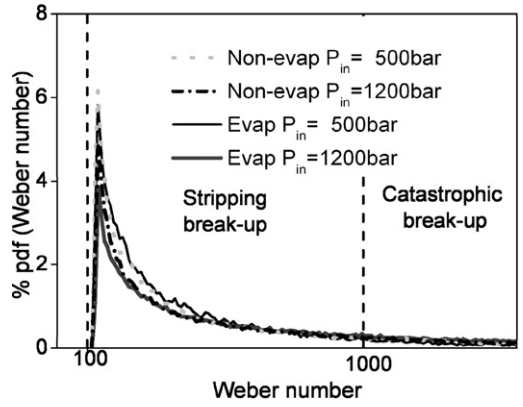

Fig. 4. Droplet Weber number distribution over the injection period under non-evaporating and evaporating conditions for two nominal rail pressure values of 500 and 1200 bar; case 9a of Table 2.

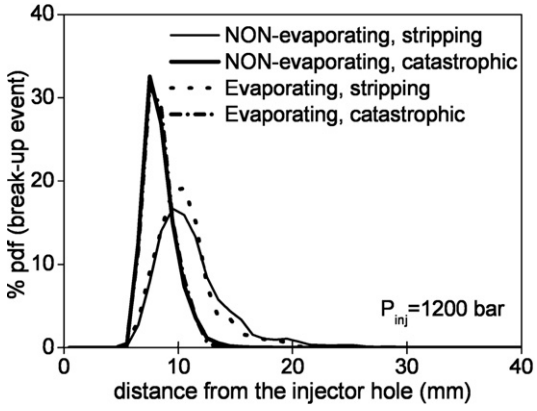

Fig. 5. Percentage of break-up event occurrence in the stripping and catastrophic modes as function of the distance from the nozzle exit; case 9a of Table 2.

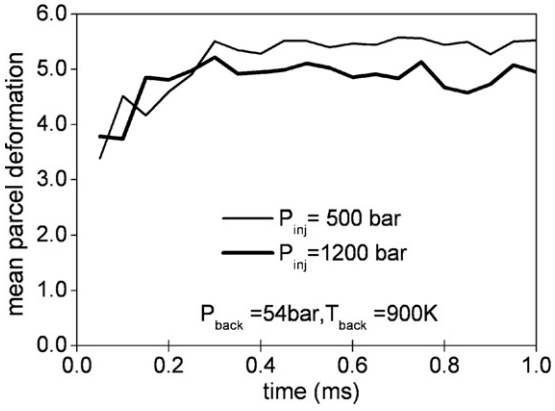

Fig. 6. Temporal variation of mean droplet deformation for two nominal injection pressures; case 9a of Table 2.

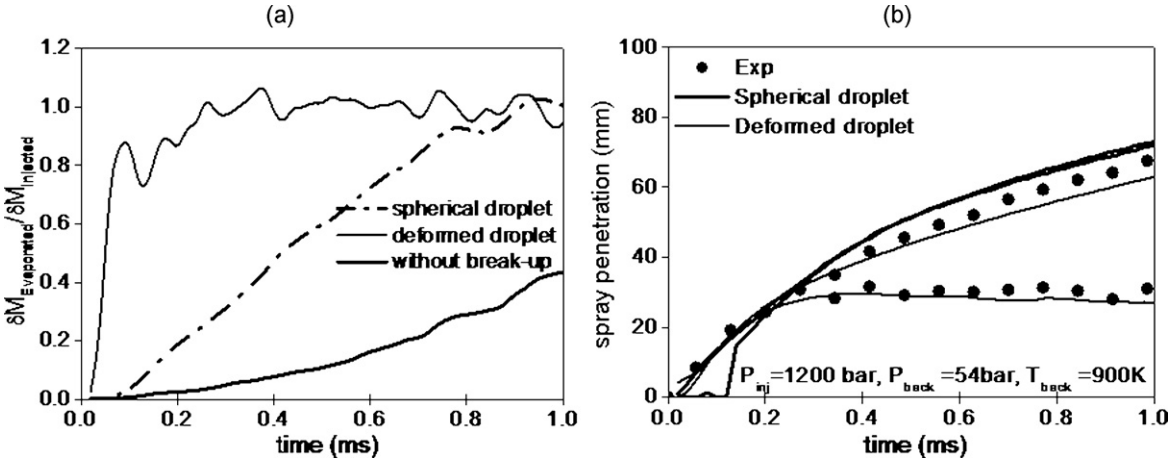

Fig. 7. Effect of droplet deformation on the temporal variation of (a) fuel vaporisation rate and (b) liquid and vapour penetration; case 9a of Table 2.

has been normalised with the instantaneous injection rate; this normalisation is responsible for the observed fluctuations of the curves of Fig. 7(a). As can be seen, the normalised vaporisation rate becomes around 1 at about 0.25 ms ASOI (After Start of Injection), in case of deformed droplet due to break-up, which implies that at this point the injection rate equals the vaporisation rate and thus, liquid penetration freezes. As can be seen, if droplet deformation is not included in the calculations or even if break-up process is not taken into account, then the time required for the fuel vaporisation to become equal to the injection rate is significantly longer, which implies that liquid penetration will not freeze at the measured distance downstream of the nozzle exit. This can be seen in Fig. 7(b) which compares the liquid and vapour penetration for the cases of considering spherical and deformed droplets with break-up. Clearly, the measured liquid penetration can be only simulated properly when deformed droplets are considered; this was a trend consistent with all cases considered.

After the pass of the break-up time, three cases are considered for calculating the *SMD* of the formed droplets. For $We < 45$, the *SMD* of the formed droplets is given by:

$$SMD = \frac{4D_p}{4 + 0.5(1 + 0.19We^{0.5})} \tag{7}$$

For these regimes, the maximum possible droplet size $D_{\max}$ required for the calculation of the droplet size distribution is assumed to be equal to the mother droplet. For the chaotic and catastrophic regimes:

$$\frac{\rho_g \cdot SMD \cdot u_{\text{rel}}^2}{\sigma_l} = C_{\text{break},1}\left(\frac{\rho_l}{\rho_g}\right)^{1/4}\left(\frac{\mu_l}{\rho_l \cdot D_p \cdot u_{\text{rel}}}\right)^{1/2} We \tag{8}$$

where $C_{\text{break},1} = 6.0$ is an empirical coefficient introduced to fit the experimental data [46,48]. The maximum possible droplet size $D_{\max}$ is assumed to be equal to the mother droplet for the chaotic regime, and equal to the maximum stable diameter for the catastrophic break-up regime, which, according to [53], can be estimated from the following correlation:

$$D_{\text{st}} = We_{\text{crit}}\frac{\sigma_l}{\rho_l u_{\text{rel}}^2}\left(1 - \frac{u_{\text{fc}}}{u_{\text{rel}}}\right)^{-2} \tag{9}$$

where the velocity of the fragment cloud when the droplet breaks is calculated as:

$$u_{\text{fc}} = u_{\text{rel}}\left(\frac{\rho_l}{\rho_g}\right)^{0.5}\left(C_{\text{break},2}\tau_{\text{break-end}} + C_{\text{break},3}\tau_{\text{break-end}}^2\right) \tag{10}$$

$C_{\text{break},2}$ and $C_{\text{break},3}$ are empirical constants equal to 0.375 and 0.236, respectively. A different approximation is introduced for the calculation of the droplet size in the stripping regime ($100 < We < 1000$). The mass flux forming the daughter droplets is estimated from the correlation:

$$\frac{dm_{\text{strip}}}{dt} = C_{\text{break},4} \cdot \rho_l\left(\frac{\rho_g}{\rho_l}\right)^{1/3}\left(\frac{\mu_g}{\mu_l}\right)^{1/6}\mu_l^{1/2}u_{\text{rel}}^{1/2}D_p^{3/2} \tag{11}$$

where $C_{\text{break},4}$ is an empirical constant set equal to 12; details can be found in [55], while the maximum possible droplet size $D_{\max}$ equals that of the mother droplet. Having determined the mean and maximum size of the formed droplets, the droplet size considered in the calculations is randomly sampled from a distribution function satisfying the maximum entropy formalism [56]. The temporal variation of the whole spray SMD shown in Fig. 8 reveals that droplet break-up reduces the mean droplet size to about half compared to that resulting from the disintegration of the liquid core. This difference results in significantly retarded vaporisation rate, as previously shown in Fig. 7(a), while liquid is found in locations far downstream of the nozzle exit.

3.4. Droplet vaporisation

Modelling of droplet evaporation plays an important role in spray calculations. Heat for evaporation is transferred to the droplet surface by conduction and convection from the surrounding hot gas and vapour is transferred by convection and diffusion back into the gas steam. The conservation equations governing the temporal evolution of global droplet quantities during the evaporation process are the conservation of total droplet mass:

$$\frac{dm_p}{dt} = \dot{m}_p \tag{12}$$

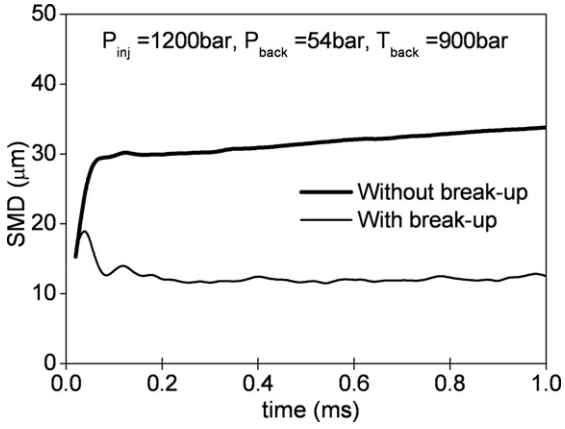

Fig. 8. Effect of break-up model on spray SMD; case 9a of Table 2.

with the vaporisation rate $\dot{m}_p$ taken positive when the droplet looses mass, and the conservation of energy for the droplet:

$$\frac{d}{dt}(m_p Cp_l T_l) + \Delta H \frac{dm_p}{dt} = 4\pi R_p^2 h(T_g - T_l) \tag{13}$$

Different models have been introduced to model the change of droplet size, temperature and composition during the vaporisation process. The rates of heat and mass transfer are affected by the droplet Reynolds number. Here, the correlation proposed by [57] expressing the vaporisation rate is used:

$$\frac{dm_p}{dt} = \pi \cdot D_p \cdot \rho_{g,\mathrm{ref}} \cdot diff_{g,\mathrm{ref}} \cdot Sh \cdot \log(B_M) \tag{14}$$

where the gas phase density and diffusivity, $\rho_{g,\mathrm{ref}}$ and $diff_{g,\mathrm{ref}}$, are calculated at reference conditions, according to [58] and Sh is the mass transfer rate defined by the Sherwood number:

$$Sh = \left(2 + \frac{0.6 \cdot Re^{1/2} \cdot (\mu_{g,\mathrm{ref}}/\rho_{g,\mathrm{ref}} \cdot diff_g)^{1/3}}{(1+B_M)^{0.7}(\log(B_M))/B_M}\right)\frac{\log(B_M)}{B_M} \tag{15}$$

Many studies have been performed on the modelling of single droplet evaporation; for a general review refer to [59] and [34]. Most of them assume steady-state conditions and spherical single-component liquid droplets. Since unsteady convection effects have been found not to affect significantly the heat transfer coefficients, most models assume quasi-steady-state conditions around the droplet and use empirical correlations for the heat and mass transfer coefficients. A number of studies address the evaporation of multi-component fuels, for example [60] and [61]. In this case, internal droplet circulation effects, temperature variation within the droplet, diffusion effects between the different compounds and solubility effects need to be considered [42]. Another complication to the modelling of evaporation results from pressure (solubility) and superheating effects at the critical point [62]. Here, three different models are used to calculate the fuel vapour concentration at the liquid/gas interface. The first one assumes ideal phase equilibrium; the Clausius–Clapeyron equation is used to evaluate the vapour pressure at droplet surface while the equilibrium mole fraction of the vaporised species is given by:

$$Y_{i,g,\mathrm{surf}} = Y_{i,l,\mathrm{surf}} \frac{P_{\mathrm{atm}}}{P_g} \exp\left[\frac{\Delta H_i mw_i}{R^*}\left(\frac{1}{T_{b,i}} - \frac{1}{T_l}\right)\right] \tag{16}$$

where R^* is the universal gas constant, $T_{b,i}$ is the liquid phase normal boiling temperature, mw_i the molecular weight and ΔH_i the latent heat of vaporisation of the fuel species i. The second model assumes non-equilibrium conditions at the liquid/gas interface. In [63] the non-equilibrium Langmuir–Knudsen evaporation law has been proposed. The effect of non-equilibrium conditions on the vapour mole fraction at the droplet surface is calculated according to:

$$Y_{i,g,\mathrm{surf,non\text{-}eq}} = Y_{i,g,\mathrm{surf}} - \left(\frac{\Lambda_K}{0.5D_p}\right)\beta \tag{17}$$

where Λ_K is the Knudsen layer thickness; the correlations for its calculation, together for the parameter β can be found in [63]. The third model states that under high-pressure conditions the assumption of ideal mixing is no longer valid. Gas solubility in the liquid-phase and variable thermo-physical properties depending on pressure, temperature and composition can be estimated by modelling the thermodynamic equilibrium for each species in the mixture in terms of the fugacity coefficients, ϕ:

$$\phi_{i,l} Y_{i,l} = \phi_{i,g} Y_{i,g} \tag{18}$$

where $Y_{i,l}$ is the mole fraction of species i in the liquid phase and $Y_{i,g}$ is the corresponding mole fraction in the vapour phase. Usually a cubic equation of state is used, for example, the Peng-Robinson EOS (Equation of State):

$$P = \frac{R^*T}{V-b} - \frac{a(T)}{V(V+b)+b(V-b)} \tag{19}$$

The coefficients a and b are calculated according to [64] and [65] using mixing rules. The fugacity coefficients can be evaluated by an equation of state explicit in pressure, function of the compressibility factor Z:

$$\ln\phi_i = -\int_{\infty}^{V}\left[\left(\frac{\partial P}{\partial N_{f,i}}\right)_{T,V,f,j\neq i} - \frac{R^*T}{V}\right]dV - R^*T\ln Z \tag{20}$$

An iterative method is required to obtain the equilibrium mole fraction defined in the matrix (18), once the compressibility factor and the fugacity coefficients are calculated. The fugacity method can be used to estimate the enthalpy for the phase change for each species in the mixture:

$$\Delta H_i = \frac{R^*T^2}{mw_i}\frac{\partial}{\partial T}\left(\ln\frac{\phi_{i,g}}{\phi_{i,l}}\right) \tag{21}$$

For the derivation of all the above models spherical droplets have been considered. However, due to their deformation, the area of the droplets in contact with the gas is greater than that of the spherical ones. Despite the fact that large deviation from the sphericity are expected according to correlation (6), no detailed mathematical model has been reported on vaporising non-spherical droplets, since for this approach the transiently varying droplet shape complicates the physical and mathematical formulation. To account for this effect and in the absence of a detailed physical model for accounting the increased heat flux resulting from the droplet shape deviation from the spherical one, a new but simple mechanism has been assumed here. That

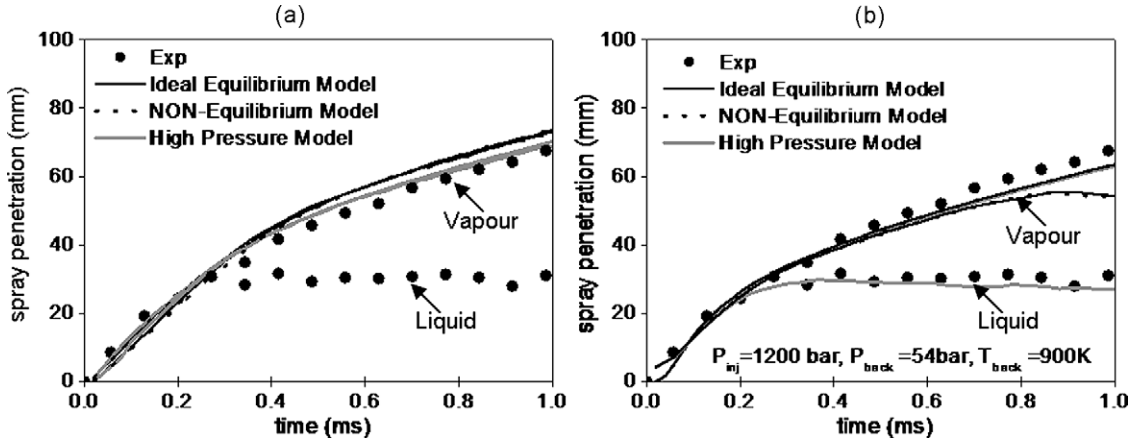

Fig. 9. Effect of evaporation model on temporal evolution of liquid and vapour penetration assuming (a) spherical droplets and (b) deformed droplets; case 9a of Table 2.

considers the inter-phase area between the two phases equal to that of a spheroid having its maximum and minimum diameters equal to those of the deformed droplet, as calculated from the break-up model:

$$A_{p,\mathrm{def}} = C_{\mathrm{def}}(D_{\mathrm{def,max}}/D_p)^2 A_{\mathrm{p,sph}} \tag{22}$$

where $D_{\mathrm{def,max}}$ is the maximum diameter of the deformed droplet, as calculated from Eq. (6), the subscript sph refers to the spherical droplet and the empirical coefficient C_{def} has to be calibrated from experiments. Introduction of this correlation into the model has been found to play major role on the development of Diesel sprays. Out of numerous studies performed as part of the model validation, the optimum value for this coefficient has been taken equal to 0.3. To demonstrate the importance of this parameter on the resulting spray, model predictions are presented for two different scenarios. In the first one, spherical droplets have been considered for estimating the contact area between the droplets and the surrounding air; the corresponding predictions are shown in Fig. 9(a). As can be seen, in this case, the vaporisation models themselves do not predict significantly different vaporisation rate in order to result in full liquid vaporisation on the measured distance downstream of the nozzle hole exit. Predictions obtained with the same evaporation models, but this time considering the increased contact area of the deformed droplets between liquid and air available for heat transfer, results in different predictions as can be seen in Fig. 9(b). The ideal equilibrium and the non-equilibrium models still fail to predict the correct trend of liquid penetration, while the high pressure model does result in increased vaporisation rate and liquid penetration similar to the measured one.

3.5. Droplet trajectory

Droplet velocity calculation is based on Newton's second law. For liquid droplets with velocities and sizes relevant to the present investigation, it has been shown by [14] and others that aerodynamic force is the dominant one with its magnitude being more than two orders of magnitude greater than the other forces. Based on that, this is the only force considered here. Numerous investigations have focused on the estimation of the drag coefficient of moving liquid droplets under a variety of conditions. In Diesel sprays, the droplets usually experience a drag that differs from that of spherical solid particles, since the flow pattern inside and around the droplet is different. Since there is no single expression for droplet drag coefficient (C_D) that applies to all conditions, the following correlations taken from [66] have been adopted here for a spherical undistorted droplet moving in a low temperature environment, taking into account the flow circulation inside the liquid droplet:

$$\begin{aligned}
&Re < 5:\\
&C_D = \frac{8}{Re}\frac{3\lambda+2}{\lambda+1}\left(1+0.05\frac{3\lambda+2}{\lambda+1}Re\right)\\
&\qquad - 0.01\frac{3\lambda+2}{Re} + 1Re\,\mathrm{Log}(Re)\\
&Re \geqslant 5, Re \geqslant 1000 \quad \Rightarrow \quad Re = 1000:\\
&C_{D,0} = \frac{48}{Re}\left(1+\frac{2.21}{\sqrt{Re}} - \frac{2.14}{Re}\right)\\
&C_{D,1} = 17Re^{-2/3}\\
&C_{D,\infty} = \frac{24}{Re}\left(1+\frac{1}{6}Re^{2/3}\right)\\
&\lambda > 0 \text{ AND } \lambda < 2\text{: } C_D = \frac{\lambda-2}{2}C_{D,0} + 4\frac{\lambda}{\lambda+6}C_{D,\infty}\\
&\lambda > 2\text{: } C_D = \frac{4}{\lambda+2}C_{D,1} + \frac{\lambda-2}{\lambda+2}C_{D,\infty}\\
&\lambda = \mu_l/\mu_g
\end{aligned} \tag{23}$$

where Re is the Reynolds number. According to [67], evaporation affects droplet drag in two ways. Firstly, the temperature and concentration gradients between the particle surface and the ambient gas cause substantial reductions in the viscosity of the gas, which reduces drag coefficient. Secondly, the mass transfer associated with droplet evaporation induces the so called 'blowing' effect, which reduces friction drag and increases form drag. These effects can be taken into account in the calculation of the drag coefficient through well established empirical correlations, for example those reported by [68]. For droplet motion in an

evaporating environment, temperature and concentration gradients and 'blowing' effects due to mass transfer influence the drag coefficient, according to the empirical correlation of [69]:

$$C_{D,\mathrm{evap}} = C_D/(1 + B_M) \tag{24}$$

where B_M is the Spalding mass transfer number, defined as:

$$B_M = \left(\sum_{i=1}^{N_{\mathrm{tot}}} y_{i,g,\mathrm{surf}} - \sum_{i=1}^{N_{\mathrm{tot}}} y_{i,g,\infty}\right) \Big/ \left(1 - \sum_{i=1}^{N_{\mathrm{tot}}} y_{i,g,\mathrm{surf}}\right) \tag{25}$$

With $y_{i,g,\mathrm{surf}}$ and $y_{i,g,\infty}$ the vapour mass fraction of the species i at the droplet surface and in the surrounding ambient, respectively. The correlation was found to be valid for droplets with in the range of 25–500 μm and for mass transfer number from 0.06 up to 12.3 [68]. In case of droplet motion in the presence of other droplets, the expression for the drag coefficient takes the following form, according to [70]:

$$C_{D,\alpha_l} = C_D \cdot \left(\exp^{2.1\cdot(1-\alpha_l)} + (1-\alpha_l)^{0.249}\right) \tag{26}$$

function of the local liquid volume fraction α_l. The relatively high velocity between the liquid droplet and the surrounding gas induces droplet deformation [50,51,55], which considerably affects the drag coefficient according to the following expression:

$$C_{D,\mathrm{def}} = C_D[0.85 + 0.15 D_{\mathrm{def}}/D_p] \tag{27}$$

where the ratio D_{def}/D_p represents the droplet deformation estimated by the break-up model, Eq. (6). Once the drag coefficient is determined, the instantaneous droplet velocity is estimated, based on Newton's second law:

$$\frac{d(m_p \mathbf{u}_p)}{dt} = \mathbf{F}_{\mathrm{tot}} = \mathbf{F}_{\mathrm{aerod}} = C_D \frac{\rho_l A_p}{2} \mathbf{u}_{\mathrm{rel}} |\mathbf{u}_{\mathrm{rel}}| \tag{28}$$

Then, the trajectory equation is integrated in time using the first order Euler integration rule in order to calculate explicitly the new droplet position.

Droplet aerodynamic drag not only affects liquid penetration, but the resulting droplet momentum loss is equal to the momentum exchange between the two decelerating droplets and the air motion induced by the spray injection. The various correlations proposed so far may predict different values of the drag coefficient, which can become important during the motion of isolated droplets. Their effect on the spray development under non evaporating conditions can be seen in Fig. 10 for the nominal rail pressure of 1200 bar. Four correlations have been tested for the purposes of the present investigation. 'Model 1' assumes spherical droplets with drag coefficient equal to that of solid particles; this is an assumption frequently adopted in a number of relevant studies, for example [68]. 'Model 2' takes into account the flow circulation inside the spherical liquid droplet through Eq. (23) and which results in decreased drag coefficient, while 'Model 3' adds a further correction to the drag coefficient of the previous correlation considering the presence of other droplets, Eq. (26), and which effectively considers motion in the wake of the droplets moving ahead and thus experiencing reduced drag. Finally, 'Model 4' considers the effect of deformed rather than spherical droplets through Eq. (27); based on visualisation studies of deforming and breaking droplets [51], the deformation is mainly normal to the droplet motion and thus the drag coefficient should be increased relative to the spherical case. Clearly only marginal differences can be appreciated in the predicted penetration curves for the non-evaporating case (Fig. 10(a)) using the four different correlations of drag coefficient. On the other hand, the results presented in Fig. 10(b) and (c) for the evaporating case, considering the effect of deformation only in the drag model or both in the drag and vaporisation models respectively, suggest that only 'Model 4', which includes the contribution of liquid droplet deformation both in drag and vaporisation rate modelling, can predict the correct trend for the liquid penetration.

3.6. Parcel turbulent dispersion and droplet-to-droplet interaction

Several studies have been reported for addressing turbulent flow effects on the dispersion of droplets. Here, the effect of three different models has been investigated; however the mathematical formulation used has been kept unchanged from the original references and it is not repeated here; only a very brief description is given. The first one is that proposed by [71]. This is the so-called 'eddy interaction model' for homogeneous isotropic turbulent flows, while a complete description of the model derivation can be found in [72]. The model states that the instantaneous velocity of the fluid phase should be calculated by adding to the mean fluid velocity, a random fluctuating component, which is sampled from an assumed distribution function. In this concept, characteristic quantities of the turbulence structure are determined from mean gas flow properties. Consequently, the random process generates a new velocity fluctuation from a Gaussian distribution function. The second droplet turbulent dispersion model considered has been reported by [73] and represents an extension of the previous model. The main algorithm to calculate the fluctuating component of the fluid velocity that the parcel 'sees' at its location is the same as in the previous model, however, the model calculates the turbulent component of the parcel velocity when the turbulence interaction period is greater than the droplet tracking time. The last model considered for accounting droplet turbulent dispersion effects is that reported by [74].

Finally, the model adopted for modelling droplet collisions and coalescence processes is the model initially reported by [75]. To resolve grid dependency problems, a modified model reported by [76] that de-couples the probability of collisions between droplets from the volume of the computational cells containing the colliding droplet parcels has been adopted. Similarly to the drag coefficient correlations, the models when applied to isolated droplets may result in different droplet trajectories, as shown in [73]; however, predictions for thousands of droplets of different sizes where the turbulent velocity is randomly selected from a Gaussian distribution function with mean value and standard deviation calculated from the turbulence model used, at every droplet tracking time step, may smooth out the differences between the models. This can be

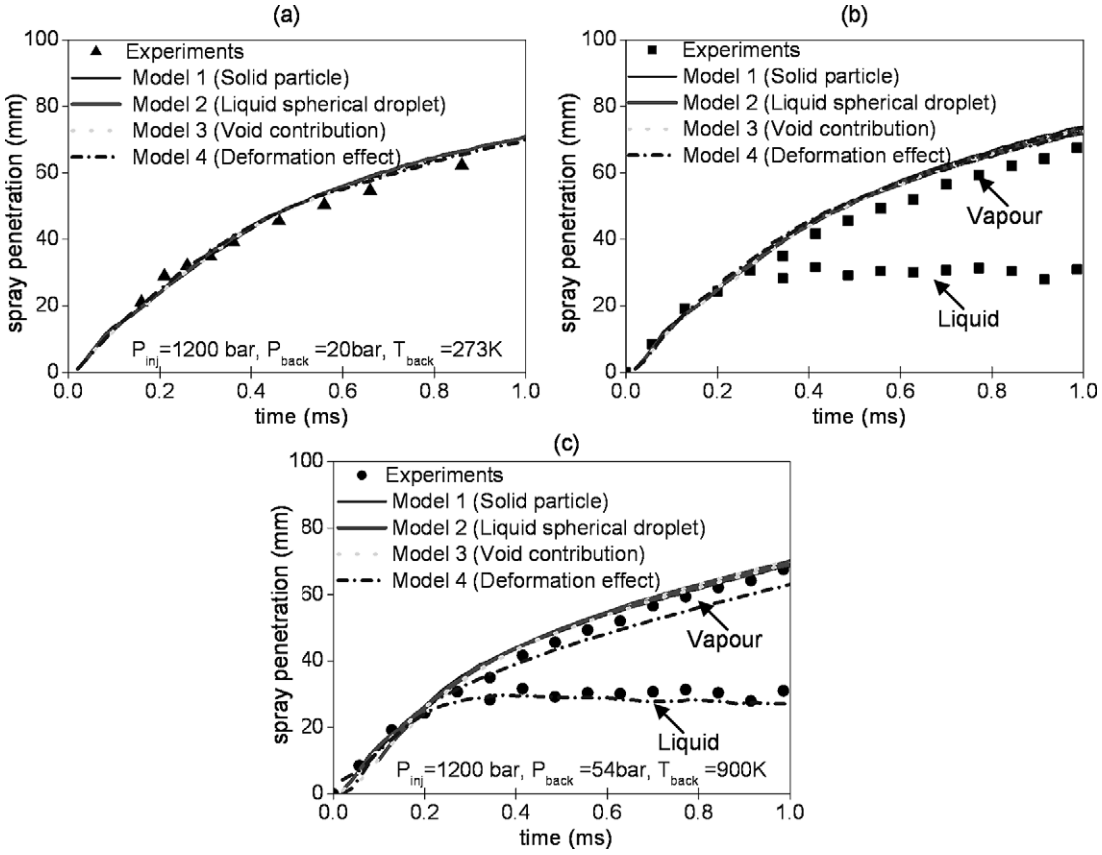

Fig. 10. Effect of drag coefficient model on temporal evolution of liquid and vapour penetration (a) non-evaporating spray, (b) evaporating spray with contact area between droplets and surrounding air based on spherical droplet shape and (c) evaporating spray with contact area between droplets and surrounding air based on deformed droplets; case 9a of Table 2.

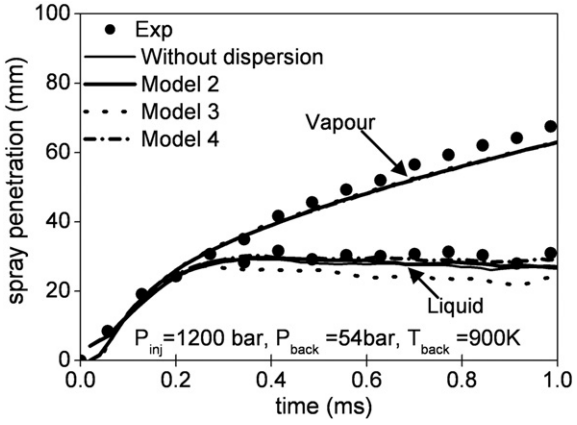

Fig. 11. Effect of droplet turbulent dispersion model on temporal evolution of liquid and vapour penetration; case 9a of Table 2.

seen in Fig. 11 for the evaporating case using the nominal rail pressure of 1200 bar. The three models of [71,73] and [74] do not result in any significant difference in the predicted liquid penetration. This is mainly because the distance travelled by the droplets until complete vaporisation and the corresponding droplet life time is rather short for turbulent dispersion processes to have any significant effect on the Diesel spray development. Predictions obtained in the absence of a turbulent dispersion model also show a very similar trend.

4. Model validation

In this section model validation for a wide range of injection and air thermodynamic conditions as well as nozzle designs is presented.

Initially, the experimental data reported in [39] have been used for model validation and include both non-evaporating as well as evaporating conditions at elevated air pressures. As mentioned in the previous section, once cavitation is forming inside the injection hole, the discharge coefficient drops while the spray momentum increases due to the associated increase of liquid velocity. To make sure that the fuel quantity is kept the same, which will be more significant for evaporating conditions, the two nozzles tested had different hole diameters. Therefore, the size of the liquid core leaving from the nozzle was different in the cases simulated, while the cavitating spray is injected with higher momentum relative to the non-cavitating one. For assessing the influence of cavitation on the injected spray, the spray tip penetration as well as droplet size have been selected for presentation. The CCD images of the non-evaporating spray shown in Fig. 12 at 1.0 ms after start of injection (ASOI) reveal a narrower and longer penetrating spray developing from the non-cavitating nozzle relative to the cavitating one for the range of injection pressures investigated; this is in qualitative agreement with model predictions. On the same graphs, the size of sample droplet parcels plotted is proportional

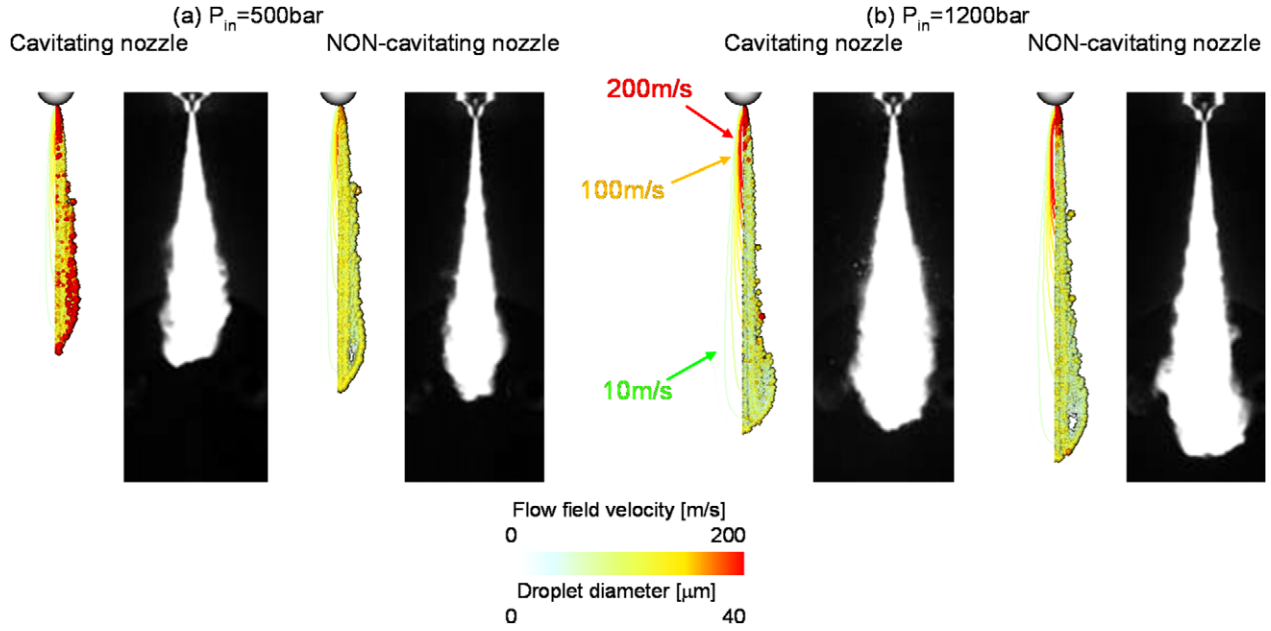

Fig. 12. Comparison between CCD images [39] and predicted structure of non-evaporating spray at 1.0 ms ASOI for the cavitating and the non-cavitating nozzles for two nominal rail pressures of (a) case 4 of Table 2 and (b) case 6 of Table 2.

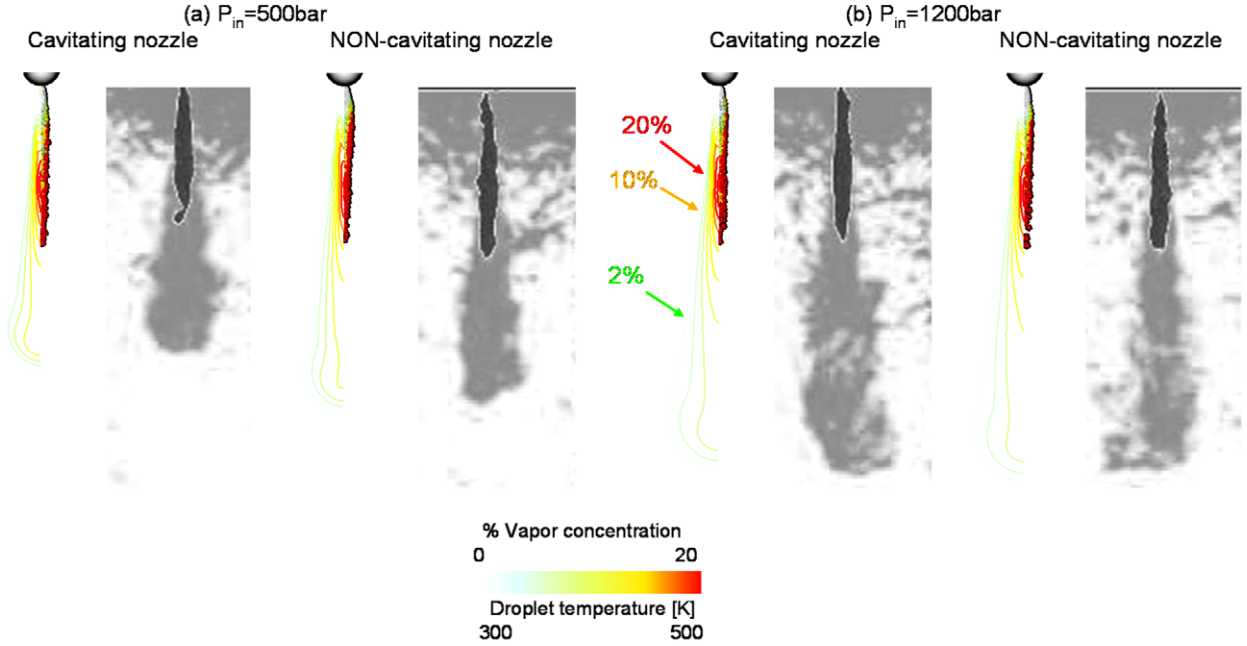

Fig. 13. Comparison between CCD images [39] and predicted structure of evaporating spray at 1.6 ms ASOI for the cavitating and the non-cavitating nozzles for two nominal rail pressures of (a) case 7, Table 2 and (b) case 9, Table 2.

to droplet diameter. As can be seen, the predicted droplet size decreases shortly after liquid injection. Droplet break-up processes also seize at a short distance of around 20 mm from the nozzle exit, as it has been described in the previous section of the paper. Evaporating conditions alter things dramatically relative to the non-evaporating ones. As can be seen in the images of Fig. 13, complete liquid vaporisation is observed after a short distance from the nozzle. This distance, usually referred to as 'liquid length' seems to be almost independent of the injection pressure, but it is a strong function of the air thermodynamic conditions. The influence of the nozzle design (cavitating versus non-cavitating) seems to be less important compared to the non-evaporating case. The penetration of both liquid and vapour is almost independent of cavitation inside the nozzle. A similar trend is also predicted by the computational model. Quantitative validation of the model is performed against experimental data for the temporal evolution of liquid and vapour tip penetration. This can be seen in Fig. 14, for the three nominal rail pressures of 500, 800 and 1200 bar, for the two nozzles tested as well as for the non-evaporating and evaporating con-

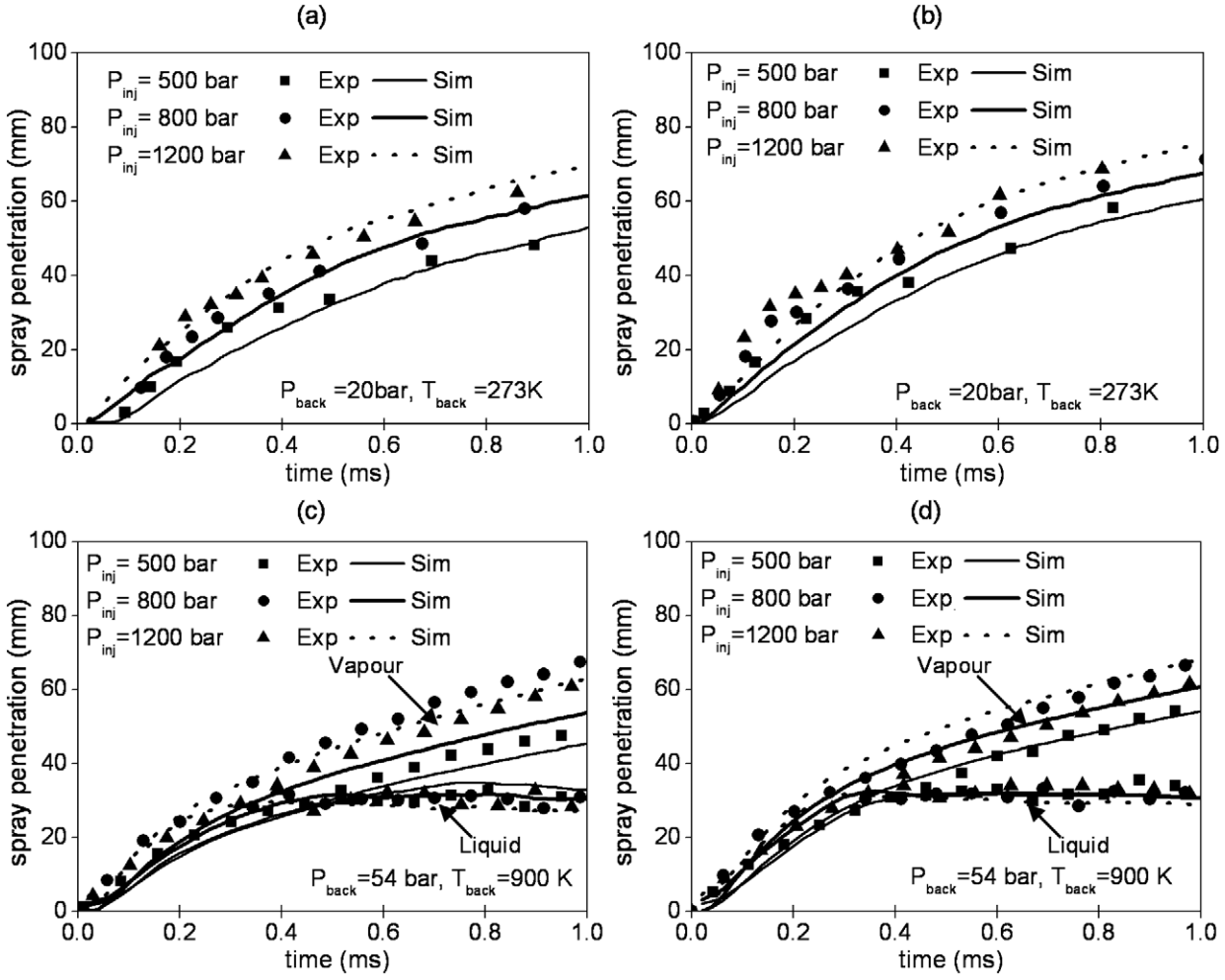

Fig. 14. Effect of injection pressure on liquid and vapour tip penetration for the test cases of Table 2: (a) cavitating nozzle under non-evaporating conditions, (b) non-cavitating nozzle under non-evaporating conditions, (c) cavitating nozzle under evaporating conditions, and (d) non-cavitating nozzle under evaporating conditions.

ditions. For non-evaporating sprays it can be seen that liquid penetrates faster with increasing injection pressure while this is not the case when evaporation is taking place. In the latter case, only vapour penetration increases with increasing injection pressure while liquid penetration is almost the same for all three injection pressures investigated. Comparison between the penetration curves of the non-cavitating and cavitating nozzles show only a small difference although the non-cavitating spray seems to penetrate slightly more. This is attributed not only to the narrower spray angle, which keeps the spray momentum concentrated on the spray axis, and thus promoting penetration, but also to the slightly larger droplet size predicted for the case of the non-cavitating spray relative to the cavitating one (not shown). Overall it can be said that the model has predicted qualitatively and quantitatively the measured trends for both nozzles and all operating conditions tested.

Further validation studies of the model have been performed against the set of experimental data of liquid length of evaporating sprays reported in [40]. The first parameter considered is the nozzle hole diameter, which has been varied from 0.1 to 0.5 mm; corresponding measurements and predictions can be seen in Fig. 15(a) for three different air temperatures using the HMN fuel while air density, injection pressure and fuel temperature have been kept fixed. As expected, decreasing nozzle hole diameter results to significant reduction of the liquid length. This is caused by the decreased droplet size resulting from smaller injection hole and which is depicted in Fig. 15(b). It is interesting to notice that despite the large difference in the nozzle hole diameter, the predicted droplet size is found in the range between 10 to 30 μm. This is mainly due to successive droplet break-up events which take place until the droplet size becomes smaller than a stable diameter. The decrease of liquid length with smaller nozzle holes is enhanced at higher gas temperatures where vaporisation is faster. The computational model reproduces the experimentally observed trends, implying that the sub-models used can be also applicable for nozzle hole sizes above the conventional ones used with passenger car Diesel engines, i.e. larger than 200 μm; this can become of practical interest, for example, with truck or marine Diesel injectors. Another parameter of significant importance is the injection pressure. Fig. 16 presents the comparison between model predictions and experimental data for the liquid length as function of the pressure drop across the nozzle hole orifice. Again, the HMN fuel is used with injection tempera-

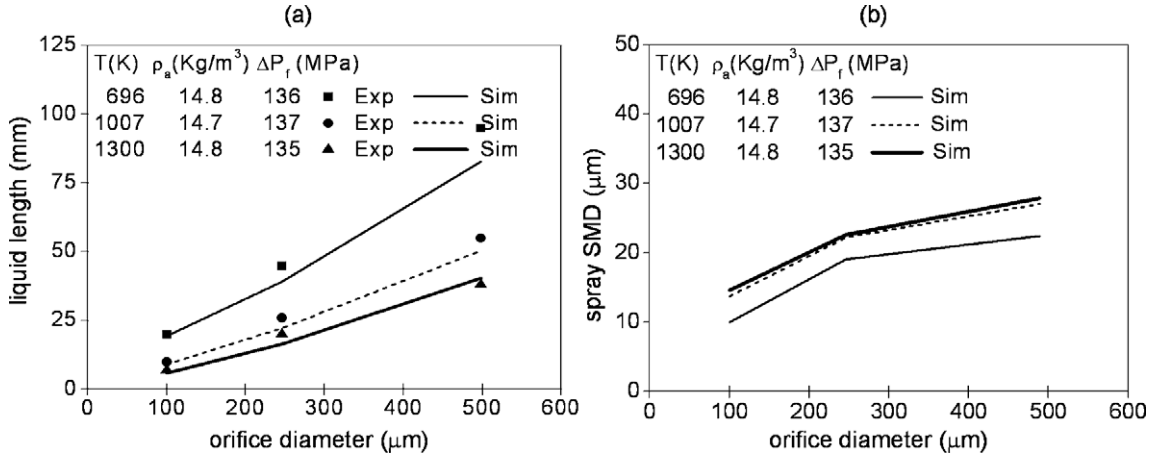

Fig. 15. Effect of orifice diameter on (a) liquid length and (b) spray SMD, for different ambient gas temperature, gas density and nozzle orifice pressure drop values, HMN fuel and 438 K injection temperature (Table 3).

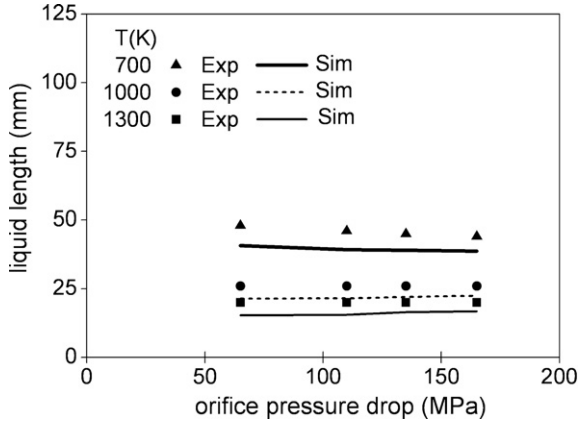

Fig. 16. Liquid length versus pressure drop across the nozzle hole orifice as function of ambient gas temperature for HMN fuel, and 438 K injection temperature (Table 3).

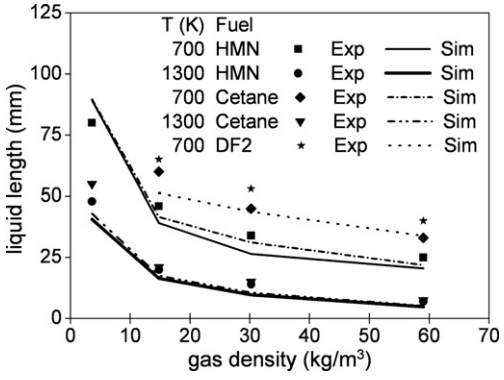

Fig. 17. Effect of fuel composition on liquid length for nozzle hole diameter 0.246 mm, HMN fuel, injection temperature 438 K and pressure drop 136 MPa (Table 3).

ture of 438 K. Results are plotted for different air temperatures but keeping the air density constant. As can be seen, injection pressure leaves the liquid length unaffected, as both predictions and experiments indicate. Since the gas density has been kept constant, the decrease of the liquid length with increasing air temperature reveals the effect of faster fuel vaporisation rather than faster spray deceleration. The effect of combined change of gas temperature, density and fuel composition is shown in Fig. 17. This time, the air pressure is kept constant. As can be seen, increasing gas density, which implies faster spray deceleration, has a profound reduction on the liquid penetration length. Again, the numerical model predicts reasonably the experimental values and trend. As already mentioned, three different fuels have been tested, namely HMN, cetane and DF2. At this point it should be mentioned that since the actual physical properties of the test fuel were not available, it is expected that model predictions may deviate from the real ones. Thus, those calculations can be interpreted as providing the correct trend with change of fuel rather than predicting the actual experimental values. It can be seen that for the low temperature case of 700 K, the heavier fuel penetrates more, while the much lighter HMN fuel exhibits a significantly reduced penetration length compared to the other two. For those cases the model predictions underestimate the experimental values of the heavy fuels by approximately 25%. This was the largest deviation between experiments and predictions from all studies performed. With increasing gas temperature, vaporisation is significantly enhanced and liquid penetration decreases. In this case, the model predictions are quite close to the experimental values. Finally, the effect of injection temperature of the cetane and DF2 fuels on liquid length is shown in Fig. 18. It can be seen that, within the range tested (380 to 440 K), liquid penetration is not significantly affected, especially at higher gas temperatures. As also seen in the previous Fig. 17, for the lower gas temperature case, the assumed fuel properties of the model result in slightly lower liquid length compared to the measured one. Overall, it can be concluded that the computational model reproduces the experimental values for the liquid penetration length over a wide range of operating conditions.

In an effort to quantify the relative influence of the parameters considered in this section, Table 6 and Fig. 19 are presented. This graph shows the standard deviation between the predicted

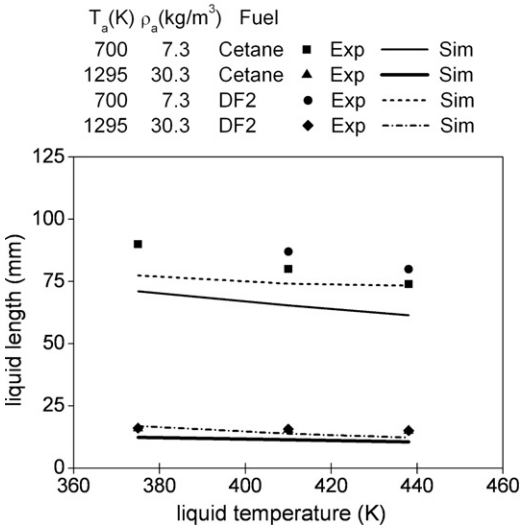

Fig. 18. Liquid length as function of initial fuel temperature for different ambient conditions for nozzle hole diameter 0.246 mm, HMN fuel, pressure drop 135 MPa (Table 3).

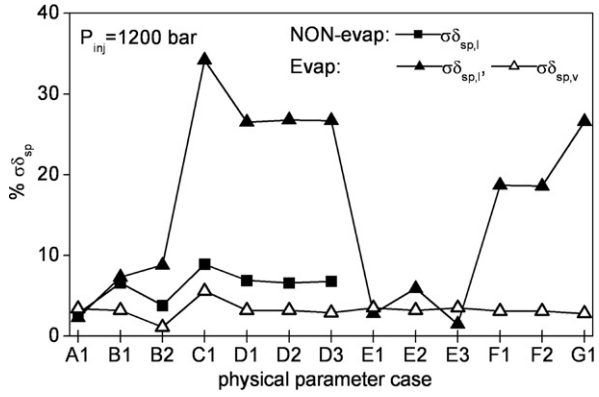

Fig. 19. Predicted time-averaged % deviation between model predictions and experimental values for the liquid and vapour penetration for the simulation cases of Table 6.

and measured liquid and vapour penetration during the spray development. This is calculated according to the equation:

$$\sigma\delta_{\mathrm{sp}} = \sqrt{\frac{1}{N_{\Delta t}}\sum_{i=1}^{N_{\Delta t}}(sp_i - \overline{sp}_i)^2} \tag{29}$$

where sp_i is the predicted spray penetration at the time-step t and $\overline{sp}_i$ the corresponding experimental value. Summation is performed up to 1.0 ms after start of injection both for the non-evaporating and evaporating sprays using the nominal rail pressure of 1200 bar. From this plot it can be concluded that remarkable deviation between simulated and measured values result mainly for the liquid penetration under evaporating conditions for the following cases: (i) when droplet break-up is not considered, (ii) when spherical droplet shape is considered in the contact area available for heat transfer and evaporation between the two phases, and (iii) when high pressure effects on vaporisation rate are not included. Model predictions for the vapour penetration are less sensitive to the different models used, since this is determined to a large extent by the momentum exchange between the two phases. For non-evaporating cases, the maximum deviation between measurements and predictions is realised in the absence of a break-up model as well as when different correlations for the drag coefficient are used.

5. Conclusions

The effect of different physical mechanisms taking place during the injection and further development of Diesel sprays has been investigated. A dense-particle Eulerian–Lagrangian stochastic methodology has been employed, able to resolve the dense spray formed at the nozzle exit using computational grids with cell volume comparable to that of the dispersed droplet parcels. The initial conditions required as input to the model have been estimated by a nozzle hole cavitation model, which predicts the injection velocity and the volumetric flow rate of the nozzle and linked with liquid core atomisation models employed for the estimation of the effect of the internal nozzle flow on the spray formation. To capture the vapour and liquid penetration of the injected spray, various vaporisation models have been tested, including high-pressure and non-equilibrium effects. Additionally, different droplet break-up and droplet aerodynamic drag correlations were used to assess the behaviour of the predicted results. The model predictions obtained have indicated that the evaporation rate of the spray at the initial stages of injection plays a crucial role in accurately calculating the liquid penetration as function of the injection pressure. The model was validated against extensive experimental data bases for the liquid and vapour penetration from different single- and multi-hole, cavitating and non-cavitating nozzles and under a variety of injection pressure, back pressure and temperature, injection hole diameter, fuel initial temperature and fuel composition. Correct trends can be predicted if the increased surface area of the droplets associated with their fragmentation process is considered during the exchange of heat and mass between the evaporating liquid and the surrounding air. Computational results have confirmed previous experimental findings on the effect of the parameters tested on liquid length of evaporating spray. The liquid penetration under high vaporisation rate conditions is nearly independent of injection pressure, while vapour penetration is higher with increased injection pressure and continuously increases with time. Liquid and vapour penetration are significantly reduced with increasing back temperature and density. Liquid penetration is linearly decreasing with nozzle hole diameter and this effect is enhanced at lower gas temperatures where vaporisation is retarded. The composition of the fuel plays a role under moderately low ambient temperature and density, where the liquid penetration has been estimated to be inversely proportional to the fuel volatility, while it seems to have minor effect under highly evaporating environments. Finally, the liquid penetration is not significantly affected by the initial liquid temperature at higher gas temperature conditions, while it linearly decreases with increasing liquid temperature at low temperature environments.

Acknowledgements

The contribution of Dr Giannadakis for the cavitating nozzle flow calculations used as input to the spray model is deeply acknowledged. The authors would like also to thank Daimler-Chrysler AG for the provision of experimental data used for validating the presented computational model and for permission to use them for the purposes of this publication.

References

[1] J.B. Heywood, Internal Combustion Engine Fundamentals, McGraw-Hill, New York, 1989.
[2] E. Giannadakis, M. Gavaises, Modelling of cavitation in large scale diesel injector, in: 19th Annual Meeting of the Institute for Liquid Atomization and Spray Systems (Europe), Nottingham, 2004.
[3] C. Soteriou, R. Andrews, M. Smith, Direct injection diesel sprays and the effect of cavitation and hydraulic flip on atomization, SAE Paper 950080, 1995.
[4] N. Tamaki, M. Shimizu, K. Nishida, H. Hiroyasu, Effects of cavitation and internal glow on atomization of a liquid jet, Atomization and Sprays 8 (1998) 179–197.
[5] M. Gavaises, C. Arcoumanis, H. Roth, Y.S. Choi, A. Theodorakakos, Nozzle flow and spray characteristics from VCO diesel injector nozzles, in: THIESEL 2002 Conference on Thermo- and Fluid-Dynamic Processes in Diesel Engines, Valencia, Spain, 2002.
[6] E. Giannadakis, Modelling of cavitation in automotive fuel injector nozzles, PhD thesis, Imperial College London, UK, 2005.
[7] H. Grogger, A. Alajbegovic, Calculation of the cavitating flow in venturi geometries using two-fluid model, in: ASME Fluids Engineering Summer Meeting, FEDSM98-5295, 1998.
[8] R. Marcer, P. Le Cottier, H. Chaves, B. Argueyolles, C. Habchi, B. Barbeau, A Validated numerical simulation of diesel injector flow using a VOF method, SAE Paper 2000-01-2932, 2000.
[9] D.P. Schmidt, C.J. Rutland, M.L. Corradini, A numerical study of cavitating flow through various nozzle shapes, SAE Paper 971597, 1997.
[10] M. Canakci, R.D. Reitz, Experimental optimization of a DI-HCCI-gasoline engine using split injections with fully-automated micro-genetic algorithms, Int. J. of Engine Research 4 (1) (2003) 47–60.
[11] Y. Liu, R.D. Reitz, Optimizing HSDI diesel combustion and emissions using multiple injection strategies, SAE Paper 2005-01-0212, 2005.
[12] P.K. Senecal, D.T. Montgomery, R.D. Reitz, A methodology for engine design using multi-dimensional modelling and genetic algorithms with validation through experiments, Int. J. of Engine Research 1 (2000) 229–248.
[13] A.A. Amsden, P.J. O'Rourke, and T.D. Butler. KIVA II—A computer program for chemically reactive flows with sprays, Los Alamos Labs, report LS 11560 MS, 1989.
[14] C. Arcoumanis, M. Gavaises, B. French, Effect of fuel injection processes on the structure of diesel sprays, SAE Paper 970799, 1997.
[15] Z. Han, L. Fan, D. Reitz, Multidimensional modelling of spray atomization and air-fuel mixing in a direct injection spark-ignition engine, SAE Paper 970884, 1997.
[16] C.F. Lee, F.V. Bracco, Comparisons of computed and measured hollow-cone sprays in an engine, SAE Paper 950284, 1995.
[17] P.J. O'Rourke, A.A. Amsden, The TAB method for numerical calculation of spray droplet break up, SAE Paper 872089, 1987.
[18] J.K. Dukowicz, A particle-fluid numerical model for liquid sprays, J. of Computational Physics 35 (1980) 229–253.
[19] S.V. Apte, M. Gorokhovski, P. Moin, LES of atomizing spray with stochastic modeling of secondary breakup, Int. J. of Multiphase Flow 29 (9) (2003) 1503–1522.
[20] A.M. Lippert, S. Chang, S. Are, D.P. Schmidt, Mesh independence and adaptive mesh refinement for advanced engine spray simulations, SAE Paper 2005-01-0207, 2005.
[21] P. Versaevel, P. Motte, K. Wieser, A new 3D model for vaporizing diesel sprays based on mixing-limited vaporization, SAE Paper 2000-01-0949, 2000.
[22] G. Bianchi, P. Pelloni, S. Toninel, D. Suzzi, D. Paganelli, A 2D simulation method for computing droplet size spectrum during the atomisation of high-speed liquid jets, in: ASME Atomisation of High-Speed Liquid Jets, ASME ICE04 Fall Technical Conference, ICEF2004-848, 2004.
[23] G. Bianchi, P. Pelloni, S. Toninel, S. Zaleski, A. Leboissetier, R. Scardovelli, A quasi-direct 3D simulation of the atomisation of high-speed liquid jets, in: ASME ICES05 Spring Technical Conference, ICES2005-1067, 2005.
[24] G. Bianchi, P. Pelloni, S. Toninel, S. Zaleski, A. Leboissetier, R. Scardovelli, Improving the knowledge of high-speed liquid jets atomization by using quasi-direct 3D simulation, SAE Paper 2005-24-0089, 2005.
[25] J.S. Han, P.H. Lu, M.C. Lai, N.A. Henein, Investigation of diesel spray primary break-up and development for different nozzle geometries, SAE Paper 2002-01-2775, 2002.
[26] E. El-Hannouny, S. Gupta, C. Powell, S. Cheong, L. Jinyuan, J. Wang, R. Sekar, Near-nozzle spray characteristics of heavy-duty diesel injectors, SAE Paper 2003-01-3150, 2003.
[27] AVL. AVL Fire Version, 8CFD WORKFLOW MANAGER v1.2, User's Guide 2003.
[28] R. Lebas, G. Blokkeel, P.-A. Beau, F.-X. Demoulin, Coupling vaporization model with Eulerian–Lagrangian spray atomization (ELSA) model in diesel engine conditions, SAE Paper 2005-01-0213, 2005.
[29] E. Platzer, M. Sommerfeld, Modelling of turbulent atomisation with a combined Euler/Lagrangian approach: starting with a two-fluid model in the dense spray region, in: ILASS-Europe 2002, Zaragoza, Spain, 2002.
[30] P.-A. Beau, M. Funk, R. Lebas, G. Blokkeel, Applying quasi-multiphase model to simulate atomization processes in diesel engines: modelling of the slip velocity, SAE Paper 2005-01-0220, 2005.
[31] S. Tonini, M. Gavaises, A. Theodorakakos, Modelling of high-pressure dense diesel sprays with adaptive local grid refinement, Int. J. Heat and Fluid Flows 29 (2008) 427–448.
[32] S. Tonini, M. Gavaises, C. Arcoumanis, A. Theodorakakos, Prediction of liquid and vapor penetration of high pressure diesel sprays, SAE Paper 2006-01-0242, 2006.
[33] S.K. Aggarwal, H.C. Mongia, Multicomponent and high-pressure effects on droplet vaporization, J. of Engineering for Gas Turbines and Power 124 (2002) 248–255.
[34] S.S. Sazhin, Advanced models of fuel droplet heating and evaporation, Prog. in Energy and Combustion Science 32 (2006) 162–214.
[35] S. Tonini, M. Gavaises, C. Arcoumanis, A. Theodorakakos, S. Kometani, Multi-component fuel vaporisation modelling and its effect on spray development in GDI engines, in: Proc. IMechE, Part D, J. Automobile Engineering 121 (10) (2007) 1321–1342.
[36] J.C. Chang, Diesel spray characteristics and spray/wall heat transfer, PhD thesis, Imperial College of Science, London, UK, 1994.
[37] P. Cutter, Diesel spray characteristics, spray/wall interactions and heat transfer, PhD thesis, Imperial College of Science, London, UK, 1997.
[38] Y.S. Choi, Diesel spray characterisation in a high-pressure chamber and in a single-cylinder engine, PhD Thesis, Imperial College of Science, London, UK, 1999.
[39] G. König, M. Blessing, Database on spray characteristics, I-LEVEL Confidential report DaimlerChrysler AG, 2003.
[40] D.L. Siebers, Liquid-phase fuel penetration in diesel sprays, SAE Paper 980809, 1998.
[41] C. Arcoumanis, M. Gavaises, Linking nozzle flow with spray characteristics in a diesel fuel injection system, Atomization and Sprays 8 (3) (1998) 307–347.
[42] S. Tonini, Fuel spray modelling in direct injection diesel and gasoline engines, PhD thesis, City University London, UK, 2006.
[43] R.D. Reitz, F.V. Bracco, Mechanism of atomisation of a liquid jet, Physics of Fluids 25 (2) (1982) 1730–1741.
[44] K.Y. Huh, A.D. Gosman, A phenomenological model of diesel spray atomisation, in: Proc. Int. Conf. Multiphase Flows, Tsukuba, Japan, 1991.
[45] C. Arcoumanis, M. Gavaises, Linking the nozzle flow with spray characteristics in a Diesel fuel injection system, Atomization and Sprays 8 (1998) 179–197.

[46] G.M. Faeth, L.-P. Hsiang, Drop deformation and breakup sue to shock wave and steady disturbances, Int. J. of Multiphase Flow 21 (4) (1995) 545–560.
[47] T.E. Su, P.V. Farrell, Characterization of high-injection pressure diesel spray with relation to particulate and NOx emissions, Atomisation and Sprays 8 (1998) 83–107.
[48] G.M. Faeth, L.-P. Hsiang, P.-K. Wu, Structure and breakup properties of sprays, Int. J. of Multiphase Flow 21 (1995) 99–127.
[49] C.A. Chryssakis, D.N. Assanis. A Secondary atomization model for liquid droplet deformation and breakup under high Weber number conditions, in: ILASS Americas, 18th Annual Conf. on Liquid Atomization and Spray Systems, Irvine, CA, 2005.
[50] L.-P. Hsiang, G.M. Faeth, Near limit drop deformation and secondary breakup, Int. J. of Multiphase Flow 18 (1992) 635–652.
[51] L.-P. Hsiang, G.M. Faeth, Drop properties after secondary breakup, Int. J. of Multiphase Flow 19 (5) (1993) 721–735.
[52] R.I. Nigmatulin, Dynamics of Multiphase Media, vol. 11, Hemisphere Publishing Corp., Washington D.C., 1991.
[53] M. Pilch, C.A. Erdman, Use of breakup time data and velocity history data to predict the maximum size of stable fragments for acceleration-induced breakup of a liquid drop, Int. J. of Multiphase Flow 13 (1987) 741–757.
[54] R.D. Reitz, R. Diwakar, Structure of high-pressure fuel sprays, SAE Paper 870598, 1987.
[55] A.A. Ranger, T.A. Nicholls, Aerodynamic shattering of liquid drops, AIAA Journal 7 (2) (1969).
[56] M. Ahmadi, R.W. Sellens, A simplified maximum-entropy-based drop size distribution, Atomization and Sprays 3 (1993) 291–310.
[57] W.E. Ranz, W.R. Marshall, Evaporation from drops, Chemical Engineering Progress 48 (1952) 141–146 and 173–180.
[58] G.L. Hubbard, V.E. Denny, A.F. Mills, Droplet evaporation: effects of transient and variable properties, International Journal of Heat and Mass Transfer 18 (1975) 1003–1008.
[59] W.A. Sirignano, Fluid Dynamics and Transport of Droplets and Sprays, Cambridge University Press, 1999.
[60] C.M. Megaridis, W.A. Sirignano, Numerical modelling of a vaporizing multicomponent droplet, in: 23rd Symposium (International) on Combustion/The Combustion Institute, 1990, pp. 1413–1421.
[61] R. Kneer, M. Schneider, Diffusion controlled vaporisation of a multicomponent droplet: theoretical studies on the importance of variable liquid properties, Int. J. of Heat and Mass Transfer 36 (9) (1993) 2403–2415.
[62] S. Hohmann, U. Renz, Numerical simulation of fuel sprays at high ambient pressure: the influence of real gas effects and gas solubility on droplet vaporisation, Int. J. of Heat and Mass Transfer 46 (2003) 3017–3028.
[63] J. Bellan, M. Summerfield, Theoretical examination of assumptions commonly used for the gas phase surrounding a burning droplet, Combustion and Flame 33 (1978) 107–122.
[64] R.H. Perry, D.W. Green, Perry's Chemical Engineers' Handbook, seventh ed., McGraw-Hill, 1997.
[65] B.E. Poling, J.M. Prausnitz, J.P. O'Connell, The Properties of Liquids and Gases, fifth ed., McGraw-Hill, 2000.
[66] Z.G. Feng, E.E. Michaelides, Drag coefficients of viscous spheres at intermediate and high Reynolds numbers, J. of Fluids Engineering-Transactions of the ASME 123 (4) (2001) 841–849.
[67] M.C. Yuen, L.W. Chen, On the drag of evaporating droplet, Combustion Science and Technology 14 (1976) 145–154.
[68] A.H. Lefebvre, Atomization and Sprays, Hemisphere, Washington, DC, 1989.
[69] P. Eisenklam, S.A. Arunachlaman, J.A. Weston, Evaporation rates and drag resistance of burning drops, in: 11th Symposium (International) on Combustion, The Combustion Institute, 1967, pp. 715–728.
[70] H. Rusche, R. Issa, The effect of voidage on the drag force on particles, droplets and bubbles in dispersed two-phase flow, in: Proc. 2nd Japanese–European Two-Phase Flow Group Meeting, Tsukuba, Japan, 2000.
[71] A.D. Gosman, E. Ioannides, Aspects of computer simulation of liquid-fuelled combustors, in: Paper AIAA-81-0323, AIAA 19th Aerospace Science Meeting, St. Louis, MO, 1981.
[72] D.I. Graham, An improved eddy interaction model for prediction of turbulent particle, J. of Fluids Engineering (Trans. ASME) 118 (1996) 819–823.
[73] P.J. O'Rourke, Statistical Properties and numerical implementation of a model for droplet dispersion in turbulent gas, J. of Computational Physics 83 (1989) 345–360.
[74] A. Stohl, D.J. Thomson, A density correction for Lagrangian particle dispersion models, Bound.-Layer Met. 90 (1999) 155–167.
[75] P.J. O'Rourke, Collective drop effects on vaporizing liquid sprays, PhD thesis, Princeton University, 1981.
[76] M. Gavaises, A. Theodorakakos, G. Bergeles, G. Brenn, Evaluation of the effect of droplet collisions on spray mixing, Proc. IMechE 210 (1996) 465–475.